Dependency of recrystallization kinetics on the solidification microstructure of 316L stainless steel processed by laser powder bed fusion (LPBF)

Edouard de Sonis[1,2], Sylvain Dépinoy[2], Pierre-François Giroux[1], Hicham Maskrot[3], Louis Lemarquis[1], Olivier Hercher[3], Flore Villaret[4], Anne-Françoise Gourgues-Lorenzon[2]*

[1] Université Paris-Saclay, CEA, Service de Recherches Métallurgiques Appliquées, F-91191, Gif-sur-Yvette, France

[2] Mines Paris, PSL University, MAT - Centre des Matériaux, CNRS UMR 7633, BP 87, 91003 Evry, France

[3] Université Paris-Saclay, CEA, Service d'Études Analytiques et de Réactivités des Surfaces, F-91191, Gif-sur-Yvette, France

[4] EDF R&D, Département Matériaux et Mécanique des Composants (MMC), Les Renardières, F-77250 Moret sur Loing, France

* Corresponding author: edouard.desonis@cea.fr

Abstract

In this study, the recrystallization kinetics of two 316L stainless steels produced by Laser Powder-Bed Fusion (LPBF) were compared. The as-built microstructures of the studied materials differed by their grain size, their grain boundary character distributions, and their populations of nanoprecipitates. Strong differences in their recrystallization kinetics were observed; they were attributed to a delayed nucleation in the steel exhibiting the finer grains, the lower density of low-angle boundaries (LAB), and the higher volume fraction of precipitates. This work shows that a high density of LABs stemming from the solidification stage in the LPBF process promotes recrystallization by locally increasing the stored energy close to grain boundaries, and hence the formation of recrystallization nuclei. The design of low-LAB microstructures could thus lead to higher stability at high temperatures.

Keywords

Recrystallization, nucleation, laser powder bed fusion, 316L stainless steel, solidification microstructure

1. Introduction

AISI 316L stainless steels possess good corrosion resistance properties due to a chromium content close to 18 % in mass [1], [2] and to their low carbon content. They are widely used in applications such as nuclear power plants, where they are present in many components of pressurized water reactors [3], as well as in automotive and aerospace industries. On the other hand, additive manufacturing techniques provide ways to produce parts that can respond to various issues encountered in these industries, such as fast prototyping, production of complex-shaped parts, manufacturing process simplification, reduction of material waste, and repairing of damaged parts [4]–[6].

In recent years, the microstructure and mechanical properties of 316L stainless steel produced by laser powder bed fusion (LPBF) have been extensively compared to those of conventionally processed grades. Namely, 316L stainless steels produced by LPBF (LPBF 316L SS) possess a unique solidification microstructure due to the high cooling rates caused by the manufacturing process [7]. Their main microstructural features are melt-pool boundaries, columnar grains with strong crystallographic texture [8]–[11], intragranular solidification cells bounded by chemical segregations [7], [12], [13], dislocation substructures [7], [14], [15] and dispersions of nanometer-sized precipitates [16]–[18]. One of the main drawbacks of such microstructures is their strong mechanical anisotropy [7], [15], [19]–[23], which can however be reduced by applying recrystallization post-heat treatments resulting in a new isotropic microstructure composed of equiaxed grains [16], [21], [24], [25]. Recrystallization is also known to improve the corrosion properties of LPBF 316L SS by homogenizing their microstructure [26], although it has been reported that the pitting corrosion resistance can drastically decline after some heat treatments at high temperatures, mainly due to the coarsening of oxide inclusions and, to a lesser extent, to the formation of MnS particles [27].

Significant discrepancies in the heat treatment conditions needed to achieve full recrystallization of this material are reported in the literature [13], [16], [21], [24], [28]–[31]. Yet, most studies aimed at obtaining recrystallized microstructures with little interest in the recrystallization scenario. Consequently, it is difficult to determine whether these discrepancies resulted from actual differences in

behavior among the heat-treated materials or from a lack of global vision of the recrystallization phenomenon. There are, however, reasons to believe that the recrystallization kinetics in LPBF 316L SS may vary to some extent owing to its well-known microstructural dependency on the LPBF process parameters [8], [32]–[35]. For instance, de Terris *et al.* showed that the LPBF processing parameters had an effect on recrystallization kinetics in Inconel 625 [36], demonstrating that using parameters leading to a high volume energy density increased the recrystallized fraction obtained after a given heat treatment.

So far, only two recent studies focused on the recrystallization mechanism of LPBF 316L SS [28], [31], the latter highlighting the difference in recrystallization kinetics between LPBF and conventionally processed 316L SS. Indeed, while Di Schino and coworkers [37] reported almost complete recrystallization of 20 % cold-rolled wrought 316L after 120 seconds at 1100 °C, the two aforementioned studies showed that the fully recrystallized state was not reached for LPBF 316L SS after 1 h at 1150 °C. Pinto and coworkers [31] attributed this sluggish recrystallization kinetics to a non-random distribution of nuclei in LPBF 316L SS, possibly due to an effect of the particular texture of these materials in the as-built state, according to Aota and coworkers [28], and to a strong pinning effect of second-phase particles slowing grain boundary migration. Two other microstructural features are also assumed to possibly hinder recrystallization in LPBF materials: (1) a low driving force due to a small difference in stored energy between adjacent grains, as observed in LPBF CM247LC by Xu and coworkers [38]; (2) the low-energy configurations of intercellular dislocations, further stabilized by chemical segregations, decreasing the mobility of dislocations at low temperatures [16], [30].

Aota and coworkers [28] compared the recrystallization kinetics of two LPBF 316L steels having two slightly different microstructures due to different scanning strategies used during LPBF processing. They observed that the material exhibiting a smaller grain size (42 ± 31 μm) and a higher fraction of high angle boundaries (HAB) recrystallized slightly faster than the material having a coarser grain structure (61 ± 43 μm) with a lower HAB density. Similar results were reported for Hastelloy X produced by LPBF [37]. However, opposite results have been reported on two LPBF 316L SS with different grain sizes by Chniouel [21] after hot isostatic pressing at 1100 °C for 3 h under 1800 bars. Indeed, he did not observe recrystallization in the steel exhibiting the finer as-built microstructure,

whereas the steel with coarser grains (grain size ratio of 3.2) was fully recrystallized. This rather uncommon and counterintuitive microstructural stability of a finer microstructure, so far unique in the LPBF literature, appears to be in direct contradiction with the results obtained in the two aforementioned studies. This shows that the recrystallization mechanisms of LPBF 316L SS are still not fully understood and that the effect of the as-built microstructural features on the recrystallization behavior of these materials remains an open question.

This present work therefore addressed the effect of the as-built microstructure on the recrystallization kinetics of LPBF 316L steel. First, two different as-built microstructures of LPBF 316L steels were produced and characterized. The recrystallization kinetics of these microstructures were then compared. The possible impact of the microstructural differences on the recrystallization kinetics is then discussed.

2. Materials and methods

56×56×56 mm^3 cubes were manufactured with an SLM Solutions 280^{HL} 3D printer from two 316L powders, the first one provided by SLM Solutions (Steel A) and the other one by Praxair (Steel B). The mean particle sizes were equal to 30 µm for both powders according to suppliers' data, and powders were systematically sieved in a 50 µm-sieve and heated up to 60 °C before use in the AM printer to remove humidity. The cubes were built under argon atmosphere using a laser power of 200 W, a beam speed of 800 mm/s, a hatch spacing of 120 µm, and a layer thickness of 30 µm. A raster scanning strategy with 7-mm-wide strips and a 67° rotation between layers was used, with additional settings regarding the orientation of the strips in relation to the argon flux to limit the slag deposition during construction. As-built cubes possessed a relative density of 99.7 %, and their chemical compositions were determined as reported in Table 1.

	Fe	**Cr**	**Ni**	**Mn**	**Mo**	**Si**	**O**	**N**	**C**
Steel A	Bal.	17.7	11.9	0.8	2.4	0.4	0.03	0.09	0.019
Steel B	Bal.	16.6	12.0	1.2	2.6	0.6	0.08	0.01	0.004

Table 1: Chemical composition of as-built cubes made of Steels A and B (in weight percent) as measured by ICP-AES for major and minor elements and by combustion analysis for trace elements (O, N, C). Relative uncertainties are 3% for major and minor elements and 10% for trace elements.

In order to investigate the microstructural evolutions at high temperature, 20×15×10 mm^3 samples were cut from the as-built parts and held under air at 1100 °C or 1200 °C for times ranging from 10 min to 4 h and subsequently water quenched. The furnace temperature was controlled by thermocouples to ensure the reproducibility of the heat treatments. The heating rate of the samples was estimated to be 800 °C/min after their introduction into the hot furnace.

After quenching, the specimens were cut along the building direction then mounted and mechanically polished with SiC grinding papers (200 to 1200-grit grades) and colloidal diamond solutions (7 to 1 µm grades) to achieve a mirror surface finish. A final polishing step with a colloidal silica suspension was applied to specimens for electron backscatter diffraction (EBSD) analysis. The samples to be observed by scanning electron microscopy (SEM) were further etched using an aqueous solution of 10 % oxalic acid by applying a 7 V voltage during 30 s. Thin foils for transmission electron microscopy (TEM) and further EBSD analyses were prepared by cutting 200-µm-thick disks from a 3-mm-diameter cylinder machined along the building direction (BD). These disks were subsequently mechanically ground down to a thickness of 120 µm and electrolytically thinned using a 45 % butoxyethanol, 45 % acetic acid, 10 % perchloric acid solution with a 30 V tension at 0 °C.

SEM observations were conducted using a ZEISS Sigma 300 field emission gun (FEG) SEM. EBSD analyses were performed with a Nordif detector using a 20 kV acceleration voltage, a 240 µm aperture, a working distance of 20 mm and a step size ranging from 0.25 to 2 µm. TEM observations were conducted using a FEI Tecnai F20 FEG-TEM with a 200 kV acceleration voltage.

The solidification cell diameters as well as the size distributions and volume fractions of nanoparticles were determined from SEM images using the ImageJ software. Solidification cell diameters were taken from the average of 1500 measurements of randomly oriented cells. Quantification of nanoparticles was performed under a 20,000 magnification over a total area of 200 μm^2, for a total

number of 800 particles in the as-built state. Data from EBSD was processed with the OIM software to directly establish (without any cleaning of the raw data) orientation and grain orientation spread (GOS) maps of the analyzed samples. GOS maps were subsequently used to calculate the recrystallized fraction f_{GOS} under the assumption that recrystallized grains exhibited a GOS lower than 1°, such that $f_{GOS} = S_{GOS<1}/S_{TOT}$, where $S_{GOS<1}$ was the area occupied by grains exhibiting a GOS lower than 1° and S_{TOT} the total analyzed surface. The dimensions of these surfaces were chosen to have the same number of grains in each analyzed sample (i.e. between 1000 and 1200 grains): 1500 × 1000 µm² for Steel A, and from 500 × 500 µm² (for non-recrystallized samples only) to 1500 × 1000 µm² (for other samples) for Steel B, the representative surface of non-recrystallized Steel B being smaller due to its smaller grain size. For this analysis, a 5° pixel-to-pixel misorientation was used to define grain boundaries, and pixels with a confidence index lower than 0.1 were not taken into account. However, the as-built microstructures of steels A and B already contained a fraction of grains that fulfilled the criterion GOS < 1°. In this non-recrystallized state, this is due to an effect of grain size on the GOS value: for a given gradient in crystal orientation, the smaller the grain size, the lower the misorientation spread, and consequently the lower the GOS [31], [40]. A correction is then necessary to give the true recrystallized fraction f:

$$f = \frac{f_{GOS} - F_{ab}}{1 - F_{ab}}, \quad (1)$$

where F_{ab} is the value of f_{GOS} in the as-built state of the considered steel, and equal to 0.04 and 0.14 for as-built steels A and B, respectively. Details about the calculation of this correction can be found in Appendix 1. Some orientation and GOS maps used for the calculation of recrystallized fractions are given in Appendix 2 and Appendix 3.

In this work, high-angle boundaries (HABs) and low-angle boundaries (LABs) were defined by pixel-to-pixel misorientations higher than 15° and between 2° and 15°, respectively.

In order to monitor softening as a function of the holding time at high temperature, Vickers hardness testing (HV_{10}) was performed on a plane parallel to BD using a load of 10 kg for 15 s. 10 measurements were carried out on each sample.

3. Results

3.1 As-built microstructures

The as-built microstructure of Steel A was composed of large columnar grains mostly oriented along the building direction (BD), with a significant <011> texture along this same direction (Figure *1*a). This grain morphology was typical of what is usually observed in LPBF 316L SS [7]–[11], [16], [41], [42]. On the other hand, Steel B exhibited smaller columnar grains and a less textured microstructure (Figure 1b).

Despite exhibiting a similar density of boundaries, there were significant differences in the nature of those boundaries depending on the considered steel (Figure 1c-d, Table 2). Indeed, half of the grain boundaries observed in Steel A were LABs, highlighted in red in the orientation maps of Figure 1a & Figure 2a and visible in the IQ map of Figure 2c. These LABs consisted of abrupt changes (by several degrees) of the crystal orientation; they delimited 2 – 10 µm-long regions where the crystal orientation varied only smoothly, as shown in Figure 2e. Voisin *et al.* reported a very similar grain structure for LPBF 316L SS and postulated that these LABs resulted from misorientations due to the melt pool dynamics during solidification, *i.e.* from boundaries between packets of solidification cells sharing a similar crystal orientation [16]. Following this assumption, these LABs will thus be referred to as solidification LABs below. The fraction of LABs was lower in Steel B (Table 2), where most grains were LAB-free as shown in Figures 2.b-d. Misorientation line plots in Figure 2.e confirmed that intragranular misorientations did not result from incremental rotations of the crystal lattice but mostly from a continuous orientation gradient. On the other hand, Steel B exhibited a larger fraction of Σ3 boundaries compared to Steel A. They were in majority incoherent twin boundaries (*Figure 1*d and Table 2). The microstructural features exhibited by steel B, *i.e*, fine grains, weak crystal texture, low LAB density and high density of incoherent twin boundaries, are rather uncommon in as-built LPBF 316L but were nonetheless reported in previous studies [19], [21], [43]–[44].

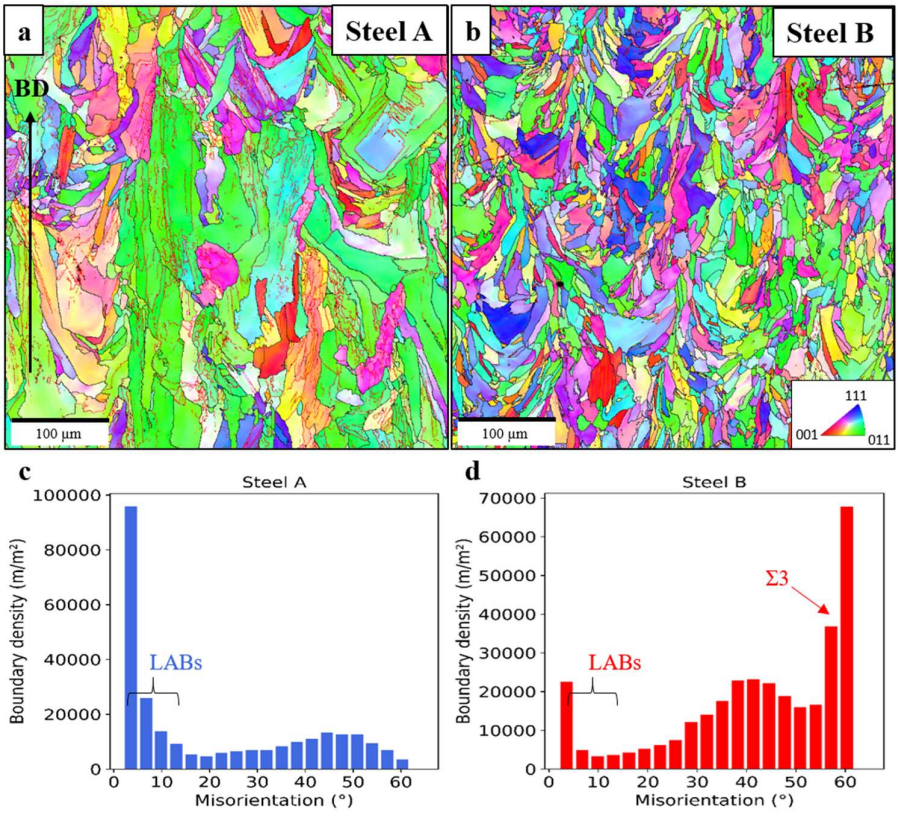

Figure 1 : Inverse pole figure maps of a) as-built Steel A and b) as-built Steel B in a plane containing BD (projection of BD in the standard triangle, step size : 0.7 µm; HABs plotted in black, LABs in red). Grain boundary misorientation density distribution for c) Steel A and d) Steel B.

Density (m/m²)	LABs	HABs	Σ3 boundaries	Total
Steel A	1.4×10^5	1.3×10^5	2.7×10^3	2.7×10^5
Steel B	3.5×10^4	2.9×10^5	8.6×10^4	3.3×10^5

Table 2: Density (m/m²) of LABs, HABs, Σ3 boundaries and total boundary density in as-built Steels A and B, as measured from EBSD maps.

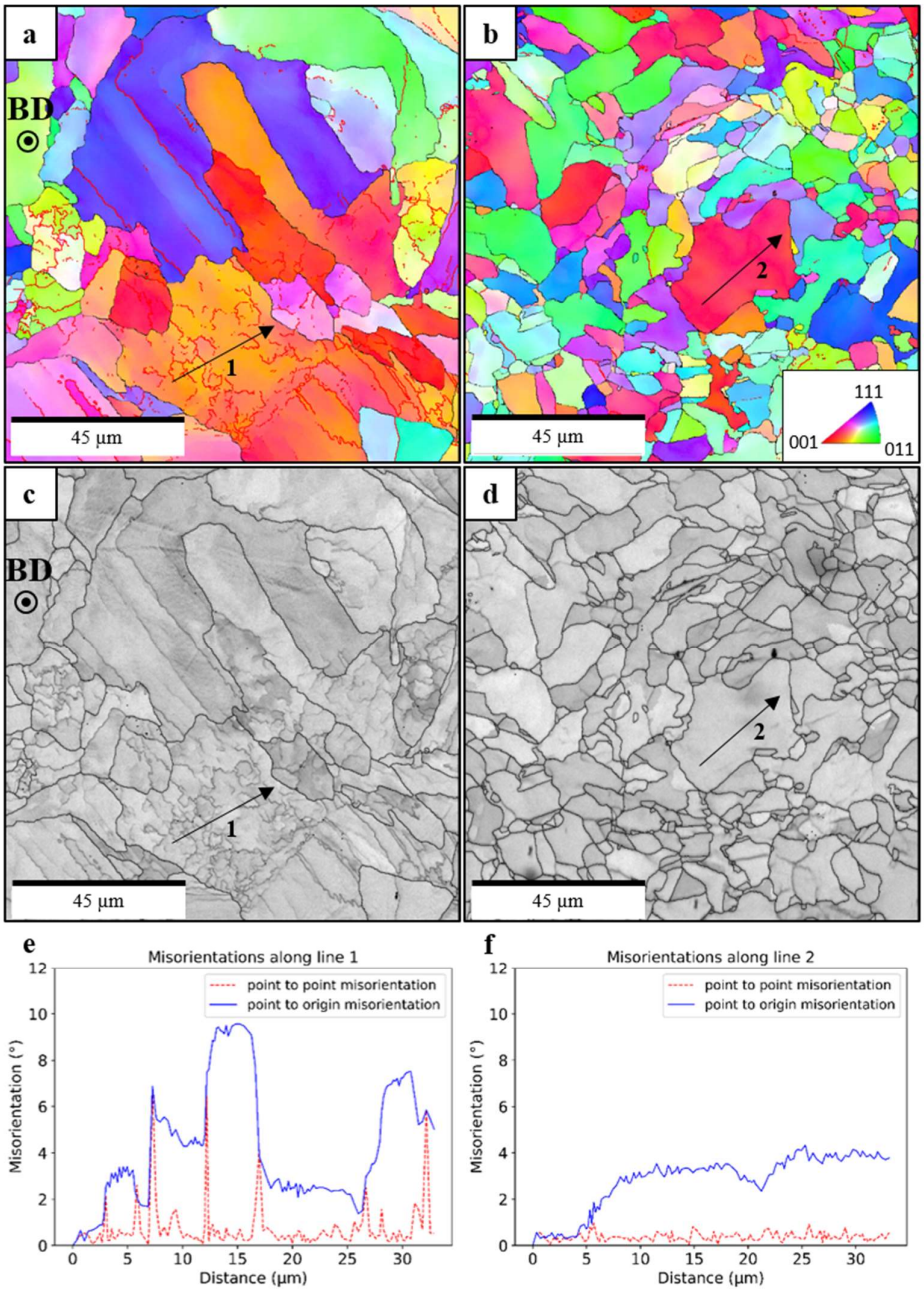

Figure 2: Inverse pole figure maps (according to BD) of a) as-built Steel A and b) as-built Steel B in the plane perpendicular to BD. HABs are plotted in black and solidification LABs in red. c) and d) Image quality maps (IQ) of the same regions with HAB plotted in black. e) and f) point-to-origin and point-to-point misorientation line plots along lines 1 and 2, respectively.

Despite these differences, both steels exhibited a similar fine-scale microstructure consisting of solidification cells (Figure 3a-b) delimited by chemically enriched intercellular boundaries (light gray in figures 3a-b). The cell diameters were 400 ± 50 nm regardless of the steel. Dislocations overlapping with cell boundaries were observed in both samples, as commonly reported for LPBF 316L stainless steels [7], [14], [16], [30], [46], [47] (Figure 3c-d). To clarify the distinctions between the different microstructural elements described in this section, the grain structure of steels A and B is schematized in Figure 4.

Nano-precipitates consistent with the manganese silicates reported in the literature [7], [16], [17], [29] were also observed. Based on their diameters, two categories of nanoparticles were identified by SEM (Figure 3), their size distributions being quantified in Figure 5. The total volume fraction of these particles was approximately 2.3 times higher in Steel B than in Steel A, namely, (0.7 ± 0.1) % and (0.3 ± 0.1) %, respectively. This ratio was similar to the ratio of oxygen contents in as-built materials (Table 1), which is known to be directly related to the number density and size of precipitates [18]. However, in the present work, the surface density of particles appeared slightly higher in Steel A (3.9×10^{12} m^{-2}) than in Steel B (3.5×10^{12} m^{-2}). This coincides with a slightly higher fraction of smaller particles in Steel A (Figure 5.a).

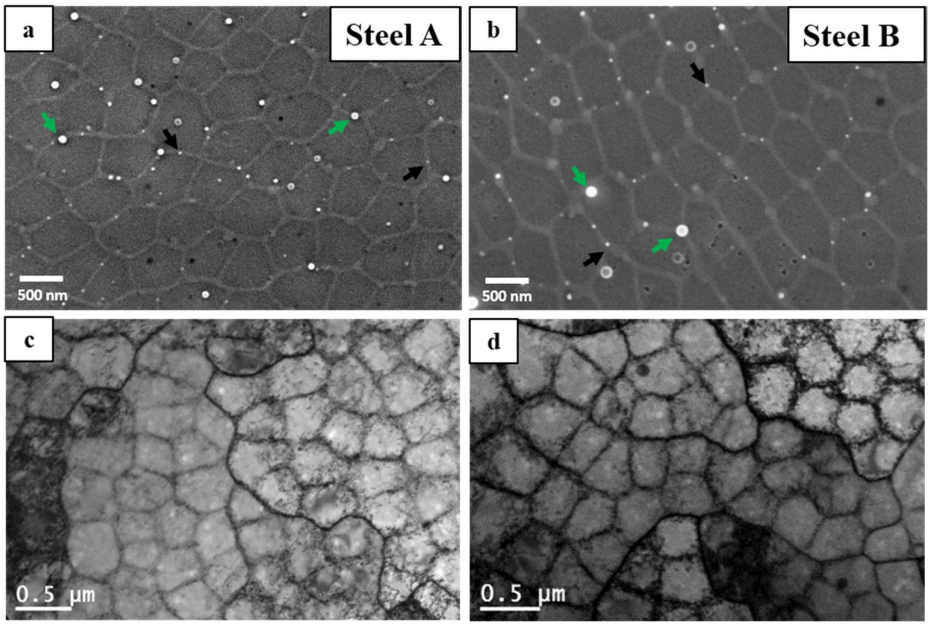

Figure 3: SEM-backscattered electron (BSE) micrographs of solidification cells and nano precipitates of a) Steel A and b) Steel B; TEM bright field images of dislocations, close to a <001> zone axis, of c) Steel A and d) Steel B. Black and green arrows respectively point to smaller and larger nano precipitates.

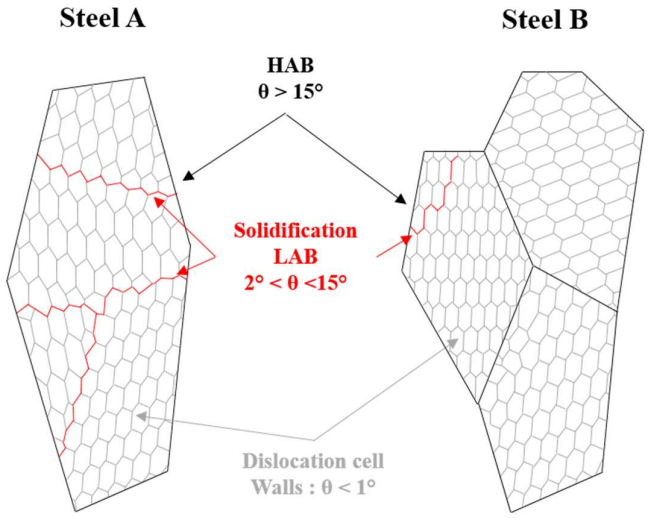

Figure 4: Schematic representation of the grain structure in Steels A and B. θ is the misorientation angle between neighboring regions.

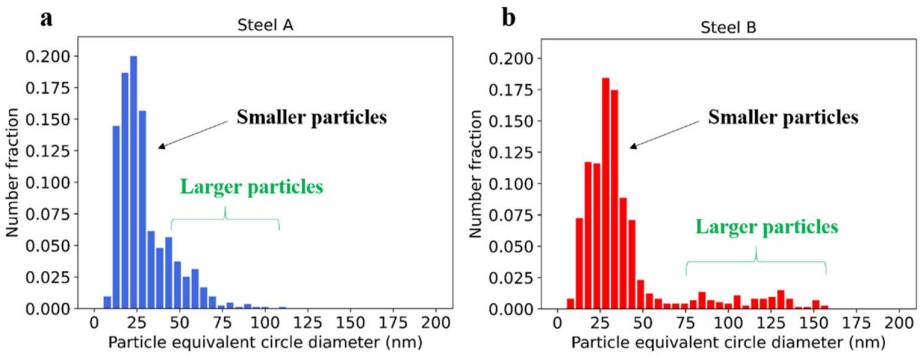

Figure 5: Equivalent circle diameter distributions of nanoprecipitates for a) Steel A and b) Steel B.

3.2 Microstructural evolution after heat treatment

3.2.1 Recrystallization kinetics

Figure 6 shows the evolution of the recrystallized fraction in Steels A and B after holding at 1100 °C and 1200 °C. Clear differences in the recrystallization kinetics of both steels can be observed: full recrystallization of Steel A was achieved after 4 h at 1100 °C, whereas no recrystallized grains were observed in Steel B after the same heat treatment (Figure 6a). Furthermore, recrystallization occurred earlier in Steel A compared to Steel B at 1200 °C (Figure 6b), although once the recrystallization had initiated, the recrystallized fraction was found to increase faster in Steel B compared to Steel A. Both steels were fully recrystallized after 1 h at 1200 °C.

3.2.2 Softening evolution

The evolution of the Vickers hardness after the heat treatments is shown in Figure 7a. Both materials experienced a decrease in hardness with holding time, with occurred faster at the highest holding temperature. While both steels showed a similar softening kinetics at 1200 °C, some differences were observed at 1100 °C. Indeed, at this temperature, the evolution of hardness in Steel A appeared consistent with its recrystallization kinetics, while the decrease in hardness for Steel B only arose from recovery, as no recrystallization took place. The hardness of heat-treated Steel B reached a plateau after 30 min holding, suggesting that recovery was complete. Figure 7b shows the decrease in hardness ($HV -$

HV_{ab}), where HV and HV_{ab} are the hardness levels of the heat-treated and the as-built steels, respectively, as a function of the recrystallized fraction. The total softening for Steel B after full recovery was 40 HV_{10}, while full recrystallization led to softening by 80 HV_{10}. Thus, the recovery phenomenon induced half of the total amount of softening for this steel. Furthermore, for both steels, the relationship between the recrystallized fraction (as evaluated from EBSD maps) and the softening (as evaluated from hardness values) was very similar, indicating that the relationships between microstructural evolution and softening kinetics were very close for both steels. Finally, a similar difference in hardness was observed between both steels both in the as-built state and after full recrystallization, i.e., 25 HV_{10}. The similar softening kinetics exhibited by both steels imply that this difference in hardness was *not* related to a difference in dislocation density in the as-built state, but rather to solid solution hardening stemming from the higher concentration of interstitial atoms in Steel B [48].

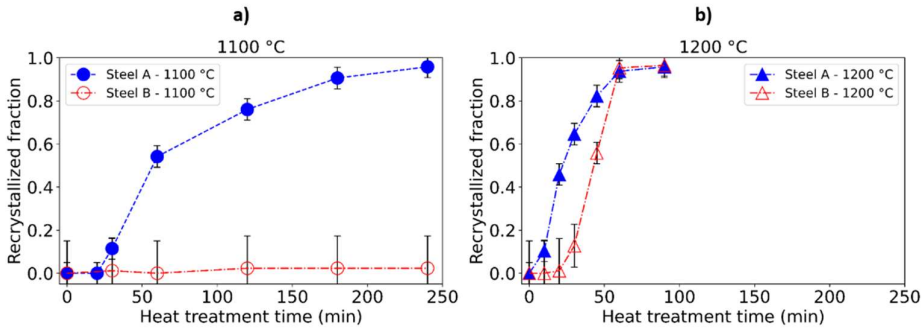

Figure 6: Recrystallization kinetics of steels A and B at a) 1100 °C and b) 1200 °C.

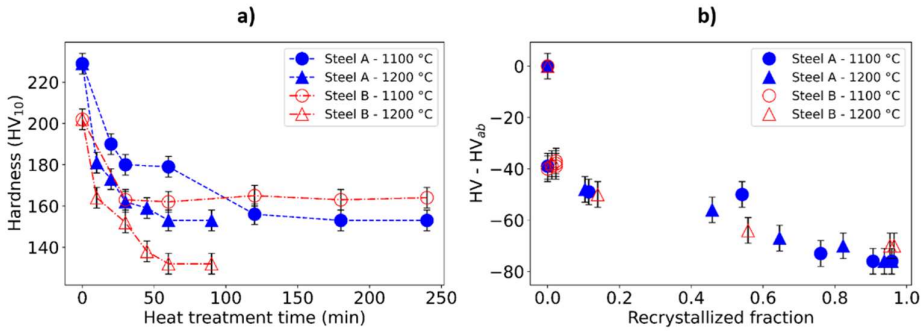

Figure 7 : a) Vickers hardness (HV_{10}) of steels A and B as function of the heat treatment time, b) Softening as a function of the recrystallized fraction.

3.2.3 Nanoprecipitates

As illustrated by comparing the orientation map of Figure 8a with the corresponding SEM image (Figure 8b) of a partially recrystallized sample of Steel A (1 h at 1100 °C), a significant fraction of precipitates was found at boundaries between recrystallized and non-recrystallized grains. These precipitates could act as pinning particles on moving grain boundaries, as previously reported for heat-treated LPBF 316L SS [28], [31], [49]. To further examine the interactions between matrix evolution and particles, the precipitate size distribution in partially recrystallized microstructures was separately quantified in recrystallized and non-recrystallized grains. Figure 8c-d shows a clear difference in particle size distribution between non-recrystallized and recrystallized grains for both steels after 30 min at 1200 °C. Non-recrystallized grains exhibited precipitates which diameters were only slightly larger than those observed in as-built material, ranging from 20 to 200 nm. On the other hand, recrystallized grains only contained coarser precipitates (200-600 nm in diameter). After almost complete recrystallization, coarse precipitates of several hundreds of nanometers in diameter were found at grain boundaries (Figure 8e-f).

3.2.4 Microstructural evolution of non-recrystallized grains

Dislocations were considerably rearranged in non-recrystallized grains, as shown by TEM micrographs of a partially recrystallized Steel B sample (1200 °C - 30 min) (Figure 9a-b). The dislocations patterns exhibited by the as-built material (Figure 3d), of 400 ± 50 nm in diameter, were replaced with dislocations structures with no particular organization (Figure 9a) and new, coarser dislocation-rich subgrain boundaries (SGB) (Figure 9b) ranging between 0.8 and 2 µm in size. These new configurations of dislocations are consistent with the full recovery of the materials during heat treatment (see the hardness curves of Figure 7a). A schematic representation of the evolution of dislocation structures under annealing is given in Figure 9e-f. Figure 10a-b show a region encompassing the area of Figure 9b, consisting of a recrystallized grain and a non-recrystallized grain as observed by EBSD and TEM. The misorientation plots of Figure 10c show that the new reorganized SGBs on the

non-recrystallized grain had a very weak misorientation within the angular resolution of EBSD, i.e., lower than 1°. On the other hand, no internal misorientation at all was detected inside the recrystallized grains (Figure 10d).

Solidification LABs remained observable in non-recrystallized grains in Steel A (Figure 9c). Their density remained higher than in Steel B and started to decrease after 10 min at 1200 °C, i.e. once the recrystallized fraction became higher than 10% (Figure 9d). On the other hand, the LAB density in Steel B tended to remain constant with time at 1200 °C before decreasing when full recrystallization was reached (Figure 9d). It can therefore be concluded that solidification LABs were not impacted by recovery but progressively disappeared due to the migration of HABs during recrystallization. Finally, both steels exhibited a similar low LABs density ($3 – 4 \times 10^4$ m/m²) after complete recrystallization.

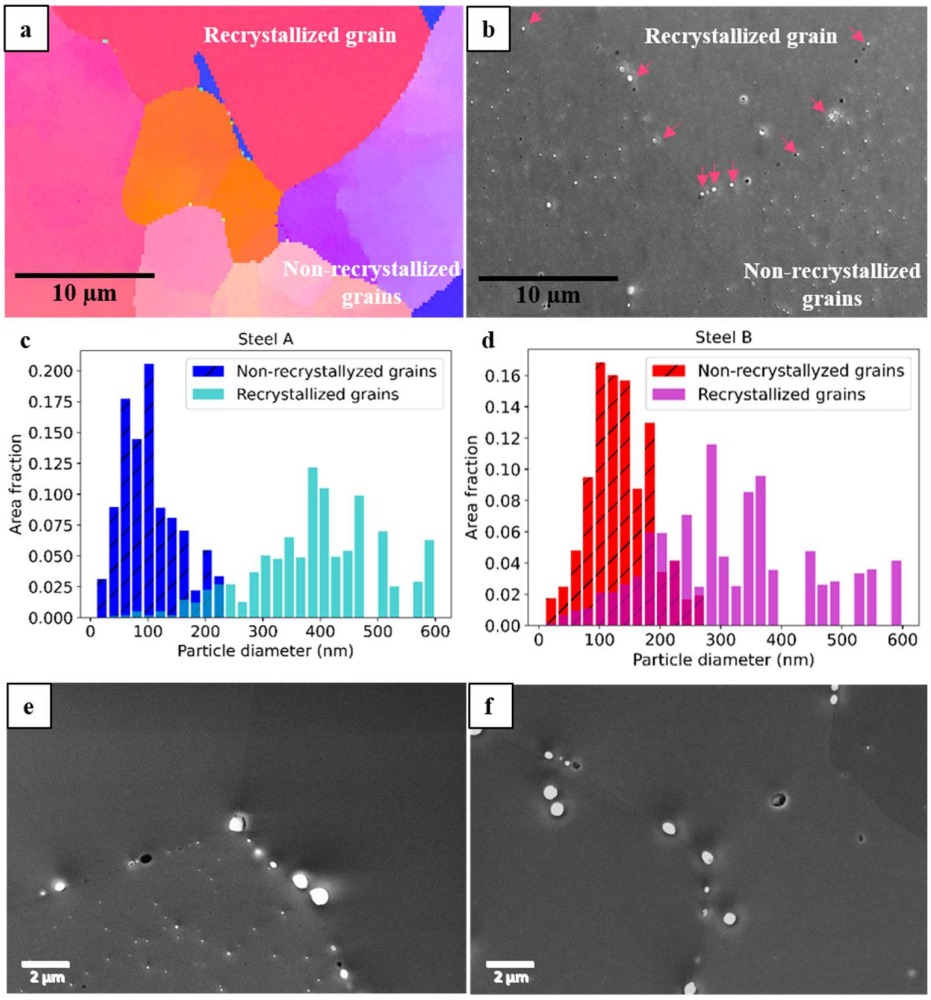

Figure 8 a) Orientation map of a partially recrystallized Steel A sample (1100 °C - 1 h) and b) corresponding SEM micrograph showing a fairly precipitate-free recrystallized grain, coarse precipitates at the recrystallization front (pink arrows), and small precipitates in non-recrystallized grains. Size distributions (in area fractions) of precipitates in non-recrystallized and recrystallized grains of c) steel A and d) Steel B after a 30 min heat treatment at 1200 °C. SEM micrographs of e) Steel A and f) Steel B after holding at 1200 °C for 1 h showing coarse precipitates at recrystallized grain boundaries.

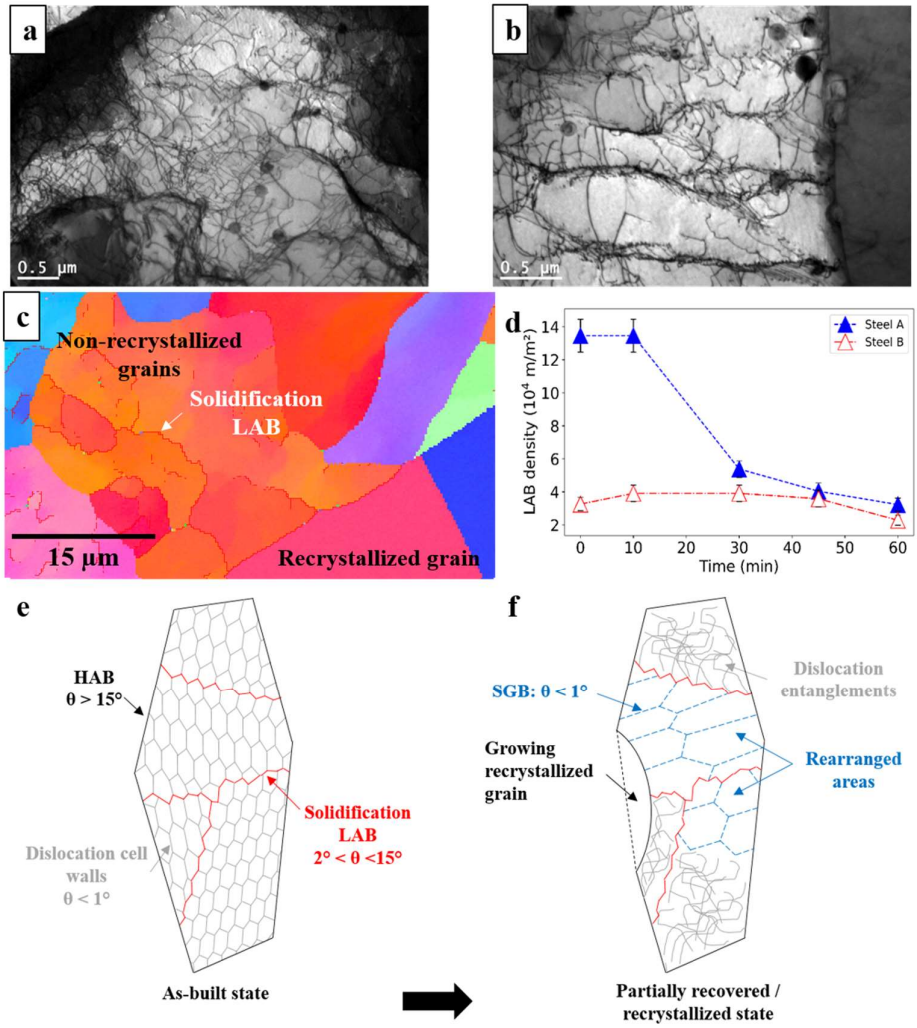

Figure 9 : Bright-field TEM images of a) a recovering area and b) a recovered area observed in a partially recrystallized Steel B sample (1200 °C - 30 min). c) Inverse pole figure map of a partially recrystallized Steel A sample (1100 °C - 1 h) with solidification LABs in non-recrystallized grains highlighted in red. d) Evolution of LAB density with holding time at 1200 °C for Steels A and B. Schematic representation of the organization of dislocations and SGBs inside grains e) in the as-built state: dislocation cells and solidification LABs, and f) in a heat-treated state leading to a partially recovered / recrystallized material: two configurations of dislocations, namely, entangled, or rearranged into new SGBs; LABs are not affected by recovery, but are no longer present after recrystallization.

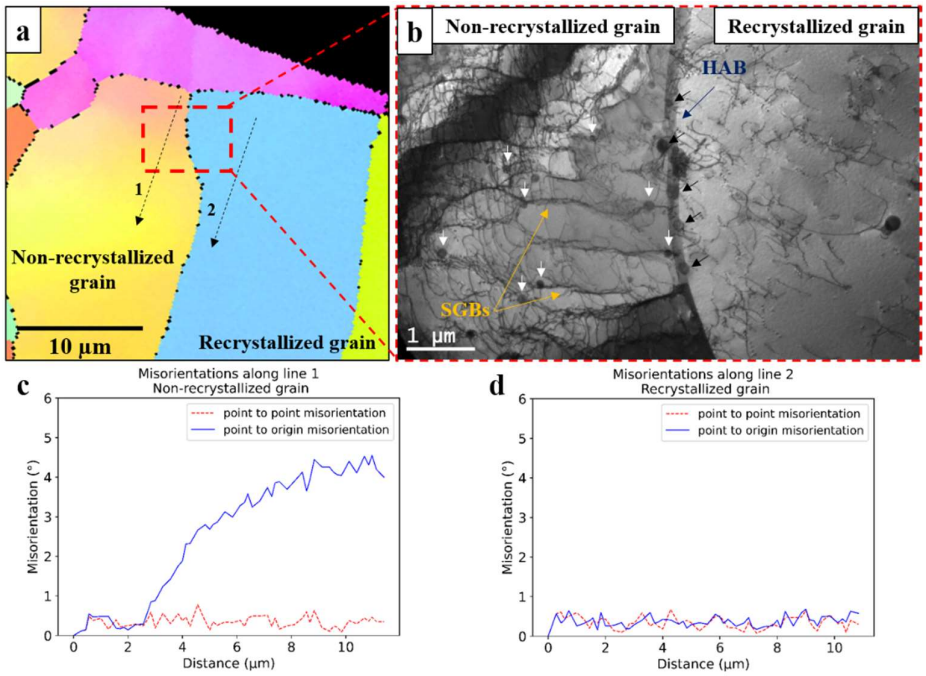

Figure 10: a) Orientation map obtained with conventional SEM/EBSD of a partially recrystallized sample of Steel B (1200 °C - 30 min), the black region being the hole of the thin foil; b) Bright-field TEM image of the red framed area of a) showing a HAB between a recrystallized grain and an un-recrystallized grain. Black and white arrows respectively indicate pinning particles at the HAB and at SGBs. c) and d) Point-to-origin and point-to-point misorientation line plots along lines 1 and 2, respectively, shown in a).

4. Discussion

The behavior of Steel A during high temperature holding corresponded to what was generally observed for 316L LPBF steels: its recrystallization kinetics was very slow in comparison to those of conventionally processed 316L SS [28], [29], [31]. The possible reasons for this have been listed in the Introduction section, namely, the stability of the as-built dislocations organization, the pinning effect of second phase particles (observed in this work: Figure 8.b and Figure 10.b) and chemical microsegregations, the particular as-built texture, and the lack of driving force for grain boundary migration. However, the unusual recrystallization kinetics of Steel B and its microstructural stability under heat treatments at high temperature, first reported by Chniouel [21] and confirmed in the present work, is so far a unique result in the literature. Possible reasons for this atypical behavior are discussed in this section.

4.1 Delayed nucleation of recrystallization in Steel B

Discontinuous recrystallization is commonly assumed to start with nucleation of a dislocation-free subgrain, which then experiences growth [50]. The delayed onset of recrystallization at 1200 °C for steel B compared to steel A (Figure 6) thus suggests sluggish nucleation in the former. In order to confirm this hypothesis, as-built Steel B samples were first heated up to 1200 °C, for a few seconds (case 1) or for 30 min (case 2) then cooled down to 1100 °C and soaked for 1 h (Figure 11). It should be recalled no recrystallization was observed for a single-step holding at 1100°C for 1 h in this steel (Figure 6a). From EBSD measurements, no recrystallization occurred for case 1, while case 2 resulted in a recrystallized fraction of 0.81. From Figure 6b, the 30-min holding at 1200 °C was expected to induce a recrystallized fraction of 0.15 (Figure 11), indicating that case 2 induced an evolution of the recrystallization fraction during the second isothermal step at 1100°C. The final recrystallized fraction in case 2 was, in fact, higher than the fraction measured in Steel A after the same holding time at 1100°C (0.56). These results show that the recrystallized fraction of steel B could increase rapidly at 1100 °C provided that recrystallization had already been triggered (case 2), but that nucleation of recrystallization was impeded at 1100°C regardless of the previous thermal history (case 1). Consequently, the lack of

recrystallization in Steel B with respect to Steel A at 1100°C was not due to a slow growth kinetics but to some inhibition of the nucleation step.

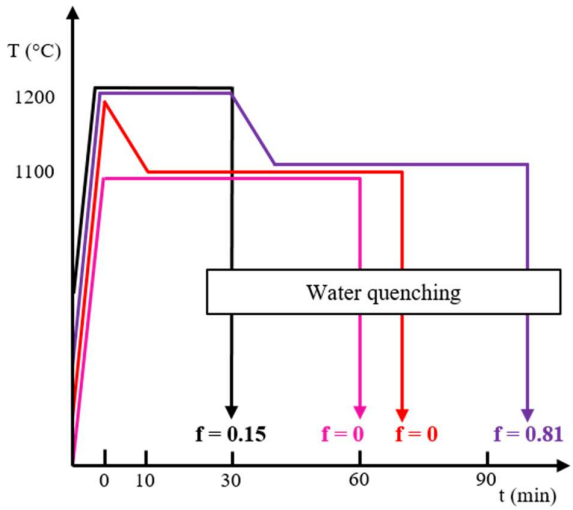

Figure 11: Different heat treatments applied to as-built Steel B and their resulting recrystallized fractions, f.

In order to further analyze this nucleation step, a hypothesis about the mechanism leading to recrystallization has to be made. Figure 12a shows a potential occurrence of strain induced boundary migration (SIBM) in Steel B after 10 min at 1200 °C, i.e., before the onset of recrystallization as detected using EBSD. This mechanism, involving the formation of a recrystallization nucleus by the bulging of a dislocation-free subgrain into a grain of high stored energy [43] [51], has been identified by Ariaseta and coworkers as the most likely recrystallization mechanism for LPBF 718 alloy [52]. Assuming that SIBM is the dominant mechanism in LPBF 316L SS, several microstructural features could hinder the nucleation step. The driving force for the formation of a recrystallization nucleus is the energy difference, ΔE, between both grains sharing a common grain boundary, as schematized in Figure 12b. The critical radius, R_{crit}, that a subgrain close to a HAB should reach in order to induce bulging, and thus to become a nucleus, is related to $\Delta E = E_2 - E_1$, where E_1 and E_2 are the corresponding stored energies on each side of the HAB, such that [53]:

$$R_{crit} = \frac{2\gamma}{\Delta E} \quad (2)$$

where γ is the energy per unit area of the HAB. Assuming thermally activated growth, a relatively dislocation-free region/subgrain of initial size R_0 and adjacent to the HAB will reach this critical radius after a time t_{inc}, hereafter referred to as the incubation time [54]. Finally, the total number of nuclei that can be activated is a direct function of the number of available nucleation sites, $\dot{N}$.

Based on the above considerations, several microstructural features can influence the incubation time. Since the intragranular dislocation density increases with the stored energy in grains, a lower dislocation density in Steel B than in Steel A, if present, could then contribute to delayed nucleation in Steel B. It has been reported that dislocation densities in LPBF-processed materials are a function of the cooling rate and of the geometrical constraints of the melt pool [14]. Both steels were built with identical processing parameters and exhibited a similar intercellular spacing, the latter being directly related to the cooling rate [55]. Consequently, no strong differences in dislocation densities were expected between the two as-built materials. This was confirmed by the overall similar organization of dislocations observed by TEM (Figure 3.c-d) and the similar softening kinetics for the two steels (Figure 7.a-b). It can therefore be safely assumed that the differences in recrystallization behavior between the two steels did not arise from differences in dislocation density.

Another important feature is the grain size or, more accurately, the density of HABs, as it is well-known that HABs are preferential nucleation sites for recrystallization [50]. The smaller grain size, and thus the higher density of HABs in Steel B, their random character linked to the absence of any pronounced texture in Steel B is expected to favor its recrystallization compared to Steel A. Since the exact opposite trend in recrystallization kinetics was experimentally observed, the grain size and the crystallographic texture did not appear to be the origin of the observed differences. A similar argument can be put forth regarding the higher density of highly mobile incoherent Σ3 boundaries in Steel B (Table 2), which is generally expected to favor recrystallization [45] [50]. In agreement with the findings of the previous section, this further implies that the observed delay in nucleation for Steel B was not due to impeded growth of already formed nuclei, which would be favored by the high mobility of HABs and

Σ3 boundaries, but by some inhibition of the formation of these nuclei, i.e., by a longer incubation time. On the other hand, the overall higher mobility of grain boundaries in Steel B may be responsible for faster growth of recrystallized grains than in Steel A at 1200 °C (Figure 6). Two other microstructural features, namely, the second phase particles and the density of solidification LABs, can also impact the incubation time. Their effects are discussed in detail in the following.

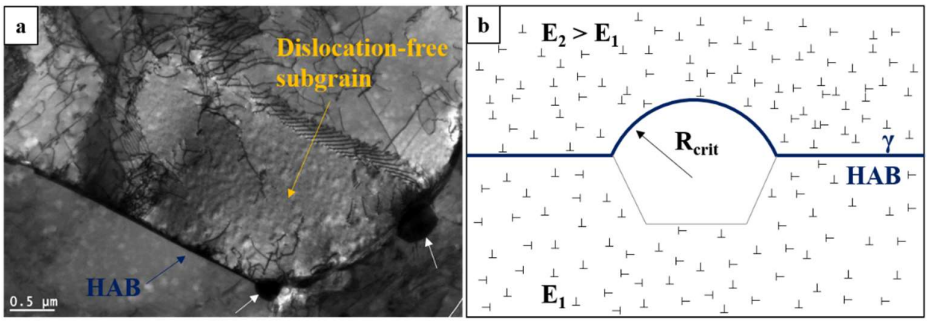

Figure 12: a) Bright–field TEM image of Steel B held at 1200 °C for 10 min showing a necessary condition for the occurrence of SIBM: formation of a fairly dislocation-free subgrain in the vicinity of a HAB. White arrows indicate a HAB pinned by precipitates. b) Schematic representation of the bulging of a dislocation-free subgrain inside a grain of high stored energy, in the framework of the SIBM mechanism.

4.2 Effect of second phase nanoprecipitates on the nucleation of recrystallization of Steels A and B

As previously stated, nanoprecipitates are a well-known cause for slow recrystallization kinetics in LPBF 316L SS due to their pinning effect on grain boundaries [28], [31], [49]. On the other hand, their potential effect on the nucleation step has not yet been highlighted in the literature. Nanoprecipitates pinning HABs, such as those pointed by white arrows in Figure 12a, are likely to slow down the bulging of HABs as already reported by Ariaseta et al for Inconel 718 [52]. It is therefore

likely that nanoprecipitates may have an inhibiting effect not only on growth, but also on nucleation of recrystallized grains.

The effect of particles on the bulging of HABs can be described by the Zener pinning pressure (P_Z), which for homogeneously distributed spherical precipitates of uniform size is given by [56] [50]:

$$P_Z = \frac{3\gamma f_v}{2r_{part}} \quad (3)$$

where f_v and r_{part} are the volume fraction and average radius of particles, respectively. Considering the case of Steels A and B, where the particles size did not obey a single-peak distribution (Figure 5), equation (3) can be rewritten as:

$$P_Z = \frac{3\gamma}{2}\sum\frac{f_v}{r_{part}} \quad (4)$$

where f_v and r_{part} respectively correspond to the volume fraction and the average radius of particles of a given class of the particle distribution, represented here by 5 nm-wide classes. It must be mentioned that equation (4) separately considers the pinning effect of each class of particles but does not take the combined pinning effect of particles of different sizes into account, and as such remain approximate. Nevertheless, taking γ = 0.7 J/m² for a HAB in 316L stainless steel [57] and the size distributions shown in *Figure 5* resulted in very close pinning pressures in steels A and B, respectively, 0.19 MPa, and 0.21 MPa. Thus, while particles may have an inhibiting effect on nucleation, it is then unlikely that they are the main factor behind the differences in recrystallization kinetics between the two studied steels.

An important consequence is that recrystallization nucleation and growth appeared to be lightly affected by an increase in oxygen concentration in the as-built material. Indeed, Table 1 shows that Steel B had an oxygen content 2.5 times higher than Steel A, leading to a higher volume fraction of oxide nanoprecipitates. However, this increase in volume fraction was mainly due to a low fraction of additional coarser precipitates and not to an increase in the total number density. This only implies a slightly higher Zener pinning pressure in Steel B compared to Steel A, and thus an overall weak variation in that contribution to the recrystallization kinetics. It follows that processing LPBF 316L SS using

oxygen-rich powder, for example recycled powder [58], may not have a strong effect on its recrystallization kinetics.

4.3 Effect of solidification LABs on recrystallization nucleation in Steels A and B

After having considered other microstructural contributions in the previous sections, the solidification LABs are thought to be the primary microstructural feature responsible for the differences in nucleation behavior between both steels. In the framework of SIBM, given by equation (2) and Figure 12b, recrystallization will start once a nucleus reaches a critical size, R_{crit}, the value of which being inversely proportional to the difference in stored energy ΔE between both sides of its neighboring HAB. A higher value of ΔE therefore lowers the value of R_{crit}, and thus promotes nucleation. Let us assume two different configurations I and II, corresponding respectively to Steels B and A and depicted in Figure 13. In configuration I, the difference in stored energy, ΔE_I, is solely due to the difference in dislocation density between both sides of the HAB. It can be further argued that ΔE_I is relatively low, as explained by Xu et al. [38], due to the nature of the LPBF process. Indeed, the dislocation density in the as-built microstructure is directly correlated to the solidification cell diameter but not on the grain orientation, and thus neighboring grains are likely to exhibit similar dislocation densities. While there is no data on the subject, it appears reasonable to assume that this remains true on recovered LPBF microstructures. The corresponding critical radius, $R_{crit,I}$, is therefore expected to be relatively large, and the incubation time relatively long. It can thus be assumed that the incubation time for Steel B was not reached after 4 h at 1100 °C and after 20 min at 1200 °C despite its high density of potential nucleation sites. On the other hand, configuration II exhibits a solidification LAB close to the HAB. The local misorientation induced by this LAB implies a higher stored energy on one side of the HAB [50], [59], and thus a higher difference in stored energy ΔE_{II} such that $\Delta E_{II} > \Delta E_I$ and, consequently, $R_{crit,II} < R_{crit,I}$. Nucleation is therefore easier in configuration II compared to configuration I, and consequently faster in Steel A than in Steel B, which is consistent with the recrystallization kinetics showed in Figure 6. Therefore, the

solidification LAB density appears to have a major contribution to the nucleation kinetics of the recrystallization of these materials. Based on these considerations, it may be possible to tune the thermal stability and the recrystallization kinetics of LPBF 316L SS by controlling the density of the solidification LABs through the processing parameters, as shown by [60], [61], for instance.

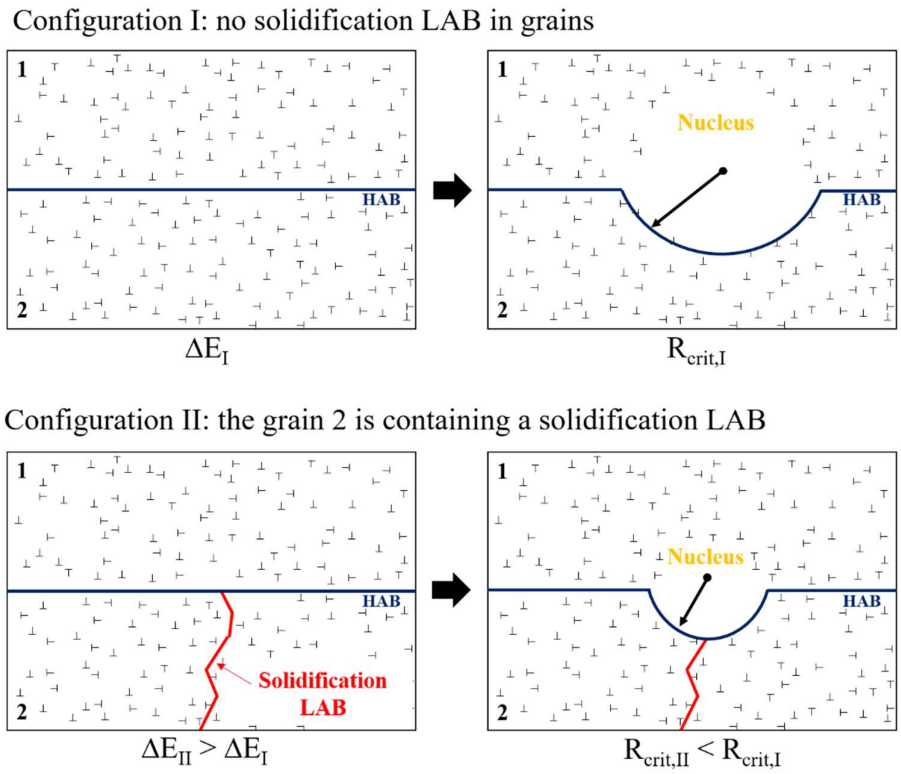

Figure 13: Proposed mechanism explaining the different nucleation kinetics between steels A and B. Configuration I (more typical of recovered Steel B): formation of a recrystallization nucleus in a zone that does not include solidification LABs. Configuration II (more typical of recovered Steel A): nucleation requiring the formation of a smaller nucleus due to the presence of a solidification LAB in one grain.

5. Conclusions

In this work, two LPBF 316L SS exhibiting significantly different as-built microstructures were heat treated at high temperature (1100 °C – 1200 °C) to assess the effect of grain size, LAB density and second phase particle distributions on the recrystallization kinetics. The main conclusions are as follows:

- A significant difference in recrystallization kinetics was observed between the two steels. Recrystallization was hindered at 1100 °C and delayed at 1200 °C for the steel exhibiting the finer grain size, the lower LAB density and the higher precipitate phase fraction. Despite its higher density of nucleation sites, the nucleation step appeared to be delayed in this steel.
- While second phase particles may have an inhibiting effect on the nucleation and growth of recrystallized grains, it is unlikely that they could explain the observed results. Increasing the oxygen concentration led to an increase in the nano-oxide phase fraction through the precipitation of coarser particles but did not significantly change the number density, leading to a similar pinning pressure.
- The difference in LAB density stemming from solidification between the two steels has been identified as a plausible cause for the difference in incubation time, as LABs are believed to locally increase the energy difference between grains at both sides of a HAB, thus promoting the nucleation of recrystallized grains by the strain induced boundary migration mechanism.
- Designing microstructures with a low LAB density could enhance the high-temperature thermal stability of LPBF 316L SS.

Data availability

The raw/processed data required to reproduce these findings cannot be shared at this time as the data also forms part of an ongoing study.

Declaration of Competing Interest

The authors declare that they have no known competing financial interests or personal relationships that could have appeared to influence the work reported in this paper.

Acknowledgements

The authors would like to thank Électricité de France (EDF) for its contribution to the financial support of this study. The authors would also like to thank all people who contributed directly or indirectly to this work, with specific thanks to N. Lochet and M. Ronfard-Haret for their technical support, and Léo Monier and Arthur Despres for the scientific discussions related to some aspects of this work.

Appendix 1: Calculation of the true recrystallized fraction, f.

$$f = f_{GOS} - F_0(f), \quad (5)$$

where f_{GOS} is the total fraction of grains exhibiting a GOS lower than 1°, and $F_0(f)$ is the fraction of non-recrystallized grains with a GOS lower than 1° in a sample having a recrystallized fraction equal to f. By defining F_{ab}, the fraction of non-recrystallized grains with a GOS < 1° in the as-built state (i.e., $f = 0$), and assuming that these grains are uniformly distributed in the analyzed sample, $F_0(f)$ can be written as $(1 - f)F_{ab}$. Consequently, the true recrystallized fraction is:

$$f = f_{GOS} - (1 - f)F_{\mathrm{ab}} \Leftrightarrow f = \frac{f_{GOS} - F_{\mathrm{ab}}}{1 - F_{\mathrm{ab}}}. \quad (6)$$

Appendix 2: Orientation and GOS maps used for the calculation of the recrystallized fraction at 1100 °C

In this appendix, some orientation maps and corresponding GOS maps of Steels A and B are given. They are a representative sample of the data sets used for the calculation of recrystallized fractions at 1100 °C.

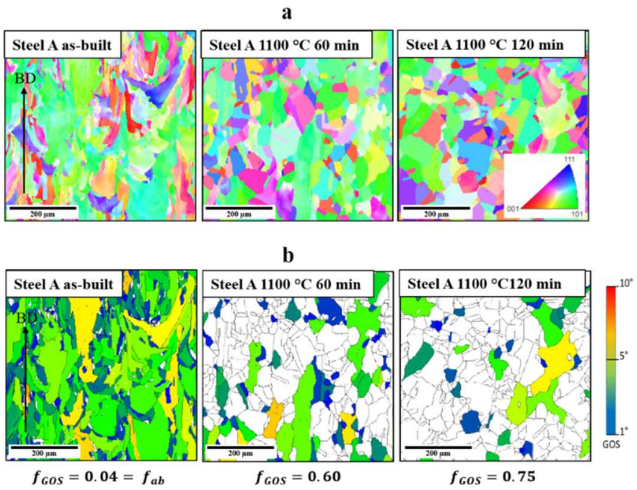

Figure A2.1: a) Orientation maps of Steel A in the as-built state and heat-treated at 1100 °C for 60 min and 120 min, b) Corresponding GOS maps used for the calculation of the recrystallized fraction f_{GOS}. Grains with a GOS<1° are displayed in white.

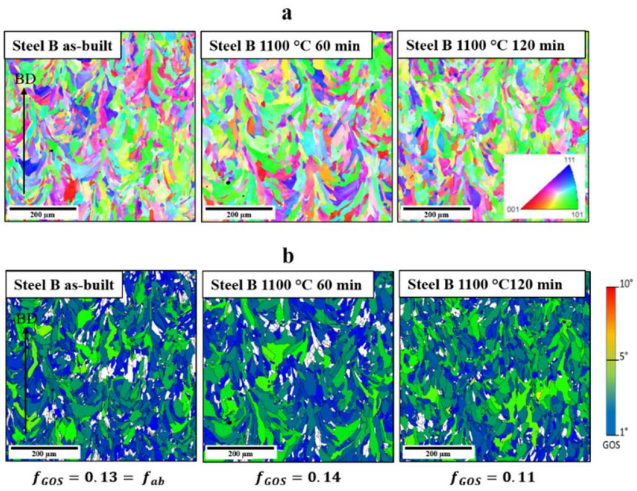

Figure A2.2: a) Orientation maps of Steel B in the as-built state and heat-treated at 1100 °C for 60 min and 120 min, b) Corresponding GOS maps used for the calculation of the recrystallized fraction f_{GOS}. Grains with a GOS<1° are displayed in white.

Appendix 3: Orientation and GOS maps used for the calculation of the recrystallized fraction at 1200 °C

In this appendix, some orientation maps and corresponding GOS maps of Steels A and B are given. They are a representative sample of the data sets used for the calculation of recrystallized fractions at 1200 °C.

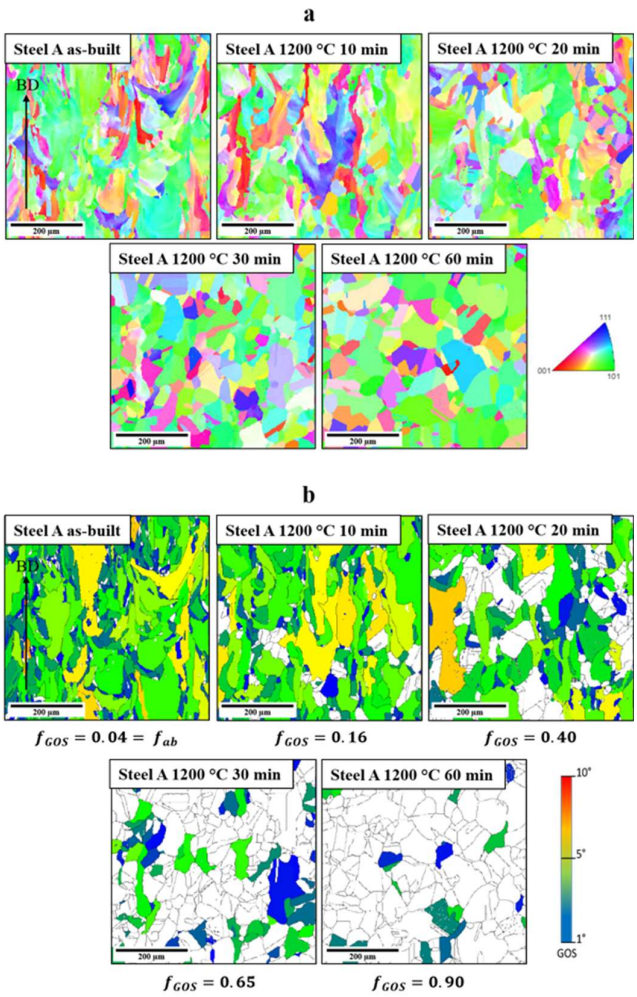

Figure A3.1: a) Orientation maps of Steel A in the as-built state and heat-treated at 1200 °C for 10 min, 20 min, 30 min, and 60 min. b) Corresponding GOS maps used for the calculation of the recrystallized fraction f_{GOS}. Grains with a GOS<1° are displayed in white.

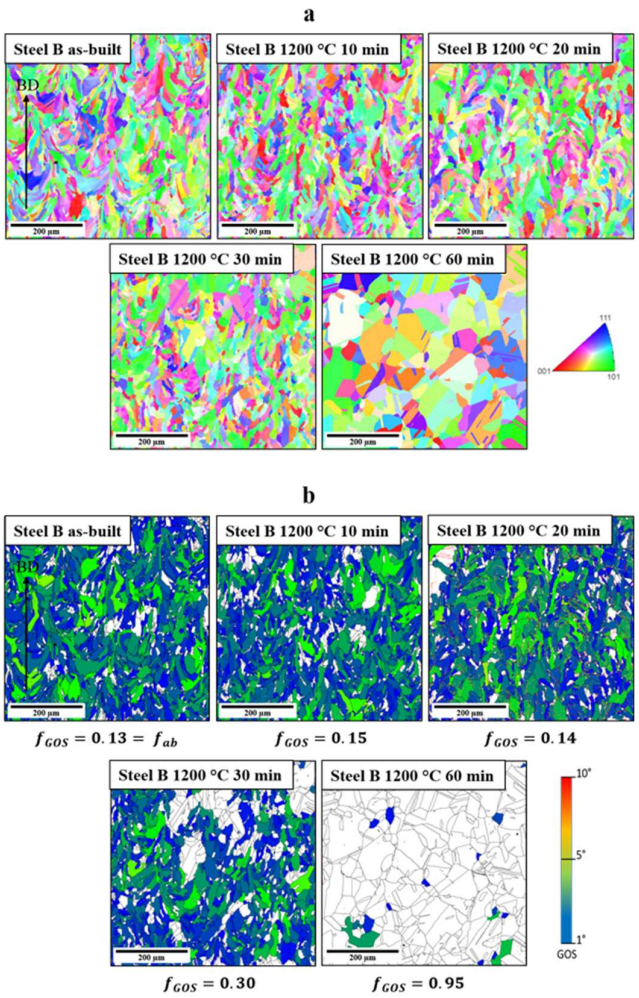

Figure A3.2: a) Orientation maps of Steel B in the as-built state and heat-treated at 1200 °C for 10 min, 20 min, 30 min, and 60 min. b) Corresponding GOS maps used for the calculation of the recrystallized fraction f_{GOS}. Grains with a GOS<1° are displayed in white.

References

[1] C.-C. Shih, C.-M. Shih, Y.-Y. Su, L. H. J. Su, M.-S. Chang, and S.-J. Lin, "Effect of surface oxide properties on corrosion resistance of 316L stainless steel for biomedical applications," *Corrosion Science*, vol. 46, no. 2, pp. 427–441, Feb. 2004, doi: 10.1016/S0010-938X(03)00148-3.

[2] E. J. Sutow, "The influence of electropolishing on the corrosion resistance of 316L stainless steel," *Journal of Biomedical Materials Research*, vol. 14, no. 5, pp. 587–595, 1980, doi: 10.1002/jbm.820140505.

[3] G. S. Was and S. Ukai, "Chapter 8 - Austenitic Stainless Steels," in *Structural Alloys for Nuclear Energy Applications*, G. R. Odette and S. J. Zinkle, Eds. Boston: Elsevier, 2019, pp. 293–347. doi: 10.1016/B978-0-12-397046-6.00008-3.

[4] L. J. Kumar and C. G. Krishnadas Nair, "Current Trends of Additive Manufacturing in the Aerospace Industry," in *Advances in 3D Printing & Additive Manufacturing Technologies*, D. I. Wimpenny, P. M. Pandey, and L. J. Kumar, Eds. Singapore: Springer, 2017, pp. 39–54. doi: 10.1007/978-981-10-0812-2_4.

[5] W. J. Sames, F. A. List, S. Pannala, R. R. Dehoff, and S. S. Babu, "The metallurgy and processing science of metal additive manufacturing," *International Materials Reviews*, vol. 61, no. 5, pp. 315–360, Jul. 2016, doi: 10.1080/09506608.2015.1116649.

[6] C. Sun, Y. Wang, M. D. McMurtrey, N. D. Jerred, F. Liou, and J. Li, "Additive manufacturing for energy: A review," *Applied Energy*, vol. 282, p. 116041, Jan. 2021, doi: 10.1016/j.apenergy.2020.116041.

[7] Y. M. Wang *et al.*, "Additively manufactured hierarchical stainless steels with high strength and ductility," *Nature Mater*, vol. 17, no. 1, Art. no. 1, Jan. 2018, doi: 10.1038/nmat5021.

[8] O. Andreau *et al.*, "Texture control of 316L parts by modulation of the melt pool morphology in selective laser melting," *Journal of Materials Processing Technology*, vol. 264, pp. 21–31, Feb. 2019, doi: 10.1016/j.jmatprotec.2018.08.049.

[9] M.-S. Pham, B. Dovgyy, P. A. Hooper, C. M. Gourlay, and A. Piglione, "The role of side-branching in microstructure development in laser powder-bed fusion," *Nature Communications*, vol. 11, no. 1, Art. no. 1, Feb. 2020, doi: 10.1038/s41467-020-14453-3.

[10] K. A. Sofinowski, S. Raman, X. Wang, B. Gaskey, and M. Seita, "Layer-wise engineering of grain orientation (LEGO) in laser powder bed fusion of stainless steel 316L," *Additive Manufacturing*, vol. 38, p. 101809, Feb. 2021, doi: 10.1016/j.addma.2020.101809.

[11] S.-H. Sun, T. Ishimoto, K. Hagihara, Y. Tsutsumi, T. Hanawa, and T. Nakano, "Excellent mechanical and corrosion properties of austenitic stainless steel with a unique crystallographic lamellar microstructure via selective laser melting," *Scripta Materialia*, vol. 159, pp. 89–93, Jan. 2019, doi: 10.1016/j.scriptamat.2018.09.017.

[12] S. Dépinoy, M. Sennour, L. Ferhat, and C. Colin, "Experimental determination of solute redistribution behavior during solidification of additively manufactured 316L," *Scripta Materialia*, vol. 194, p. 113663, Mar. 2021, doi: 10.1016/j.scriptamat.2020.113663.

[13] D. Kong *et al.*, "Mechanical properties and corrosion behavior of selective laser melted 316L stainless steel after different heat treatment processes," *Journal of Materials Science & Technology*, vol. 35, no. 7, pp. 1499–1507, Jul. 2019, doi: 10.1016/j.jmst.2019.03.003.

[14] K. M. Bertsch, G. Meric de Bellefon, B. Kuehl, and D. J. Thoma, "Origin of dislocation structures in an additively manufactured austenitic stainless steel 316L," *Acta Materialia*, vol. 199, pp. 19–33, Oct. 2020, doi: 10.1016/j.actamat.2020.07.063.

[15] L. Liu *et al.*, "Dislocation network in additive manufactured steel breaks strength–ductility trade-off," *Materials Today*, vol. 21, no. 4, pp. 354–361, May 2018, doi: 10.1016/j.mattod.2017.11.004.

[16] T. Voisin *et al.*, "New insights on cellular structures strengthening mechanisms and thermal stability of an austenitic stainless steel fabricated by laser powder-bed-fusion," *Acta Materialia*, vol. 203, p. 116476, Jan. 2021, doi: 10.1016/j.actamat.2020.11.018.

[17] F. Yan, W. Xiong, E. Faierson, and G. B. Olson, "Characterization of nano-scale oxides in austenitic stainless steel processed by powder bed fusion," *Scripta Materialia*, vol. 155, pp. 104–108, Oct. 2018, doi: 10.1016/j.scriptamat.2018.06.011.

[18] X. Zhou, Z. An, Z. Shen, W. Liu, and C. Yao, “Particles control in selective laser melting in-situ oxide dispersion strengthened method,” *IOP Conf. Ser.: Mater. Sci. Eng.*, vol. 167, p. 012048, Jan. 2017, doi: 10.1088/1757-899X/167/1/012048.

[19] T. S. Byun *et al.*, “Mechanical behavior of additively manufactured and wrought 316L stainless steels before and after neutron irradiation,” *Journal of Nuclear Materials*, vol. 548, p. 152849, May 2021, doi: 10.1016/j.jnucmat.2021.152849.

[20] R. Casati, J. Lemke, and M. Vedani, “Microstructure and Fracture Behavior of 316L Austenitic Stainless Steel Produced by Selective Laser Melting,” *Journal of Materials Science & Technology*, vol. 32, no. 8, pp. 738–744, Aug. 2016, doi: 10.1016/j.jmst.2016.06.016.

[21] A. Chniouel, “Etude de l’élaboration de l’acier inoxydable 316L par fusion laser sélective sur lit de poudre : influence des paramètres du procédé, des caractéristiques de la poudre, et des traitements thermiques sur la microstructure et les propriétés mécaniques.,” Thèse de doctorat, Université Paris-Saclay, 2019. Accessed: Feb. 08, 2022. [Online]. Available: https://tel.archives-ouvertes.fr/tel-02421550

[22] T. Ronneberg, C. M. Davies, and P. A. Hooper, “Revealing relationships between porosity, microstructure and mechanical properties of laser powder bed fusion 316L stainless steel through heat treatment,” *Materials & Design*, vol. 189, p. 108481, Apr. 2020, doi: 10.1016/j.matdes.2020.108481.

[23] A. Röttger *et al.*, “Microstructure and mechanical properties of 316L austenitic stainless steel processed by different SLM devices,” *The International Journal of Advanced Manufacturing Technology*, vol. 108, no. 3, pp. 769–783, May 2020, doi: 10.1007/s00170-020-05371-1.

[24] R. W. Fonda *et al.*, “The Effects of Post-processing in Additively Manufactured 316L Stainless Steels,” *Metallurgical and Materials Transactions A*, vol. 51, no. 12, pp. 6560–6573, Dec. 2020, doi: 10.1007/s11661-020-06039-x.

[25] P. Dong, F. Vecchiato, Z. Yang, P. A. Hooper, and M. R. Wenman, “The effect of build direction and heat treatment on atmospheric stress corrosion cracking of laser powder bed fusion 316L austenitic stainless steel,” *Additive Manufacturing*, vol. 40, p. 101902, Apr. 2021, doi: 10.1016/j.addma.2021.101902.

[26] D. Kong *et al.*, “Heat treatment effect on the microstructure and corrosion behavior of 316L stainless steel fabricated by selective laser melting for proton exchange membrane fuel cells”, *Electrochimica Acta*, vol. 276, p. 293-303, Jun. 2018, doi: 10.1016/j.electacta.2018.04.188.

[27] K. Wang *et al.*, “On the pitting behavior of laser powder bed fusion prepared 316L stainless steel upon post-processing heat treatments”, *Corrosion Science*, vol. 197, P. 110060, Apr. 2022, doi: doi.org/10.1016/j.corsci.2021.110060.

[28] L. S. Aota *et al.*, “Recrystallization kinetics, mechanisms, and topology in alloys processed by laser powder-bed fusion: AISI 316L stainless steel as example,” *Materialia*, vol. 20, p. 101236, Dec. 2021, doi: 10.1016/j.mtla.2021.101236.

[29] Q. Chao, S. Thomas, N. Birbilis, P. Cizek, P. D. Hodgson, and D. Fabijanic, “The effect of post-processing heat treatment on the microstructure, residual stress and mechanical properties of selective laser melted 316L stainless steel,” *Materials Science and Engineering: A*, vol. 821, p. 141611, Jul. 2021, doi: 10.1016/j.msea.2021.141611.

[30] L. Cui, S. Jiang, J. Xu, R. L. Peng, R. T. Mousavian, and J. Moverare, “Revealing relationships between microstructure and hardening nature of additively manufactured 316L stainless steel,” *Materials & Design*, vol. 198, p. 109385, Jan. 2021, doi: 10.1016/j.matdes.2020.109385.

[31] F. C. Pinto, L. S. Aota, I. R. Souza Filho, D. Raabe, and H. R. Z. Sandim, “Recrystallization in non-conventional microstructures of 316L stainless steel produced via laser powder-bed fusion: effect of particle coarsening kinetics,” *Journal of Materials Science*, Jan. 2022, doi: 10.1007/s10853-021-06859-1.

[32] T. Kurzynowski, K. Gruber, W. Stopyra, B. Kuźnicka, and E. Chlebus, “Correlation between process parameters, microstructure and properties of 316 L stainless steel processed by selective laser melting,” *Materials Science and Engineering: A*, vol. 718, pp. 64–73, Mar. 2018, doi: 10.1016/j.msea.2018.01.103.

[33] T. Ishimoto, S. Wu, Y. Ito, S.-H. Sun, H. Amano, and T. Nakano, “Crystallographic Orientation Control of 316L Austenitic Stainless Steel via Selective Laser Melting,” *ISIJ International*, vol. 60, no. 8, pp. 1758–1764, 2020, doi: 10.2355/isijinternational.ISIJINT-2019-744.

[34] J. J. Marattukalam *et al.*, "The effect of laser scanning strategies on texture, mechanical properties, and site-specific grain orientation in selective laser melted 316L SS," *Materials & Design*, vol. 193, p. 108852, Aug. 2020, doi: 10.1016/j.matdes.2020.108852.

[35] X. Zhang *et al.*, "Effect of the scanning strategy on microstructure and mechanical anisotropy of Hastelloy X superalloy produced by Laser Powder Bed Fusion," *Materials Characterization*, vol. 173, p. 110951, Mar. 2021, doi: 10.1016/j.matchar.2021.110951.

[36] T. De Terris, O. Castelnau, Z. Hadjem-Hamouche, H. Haddadi, V. Michel, and P. Peyre, "Analysis of As-Built Microstructures and Recrystallization Phenomena on Inconel 625 Alloy Obtained via Laser Powder Bed Fusion (L-PBF)," *Metals*, vol. 11, no. 4, Art. no. 4, Apr. 2021, doi: 10.3390/met11040619.

[37] A. Di Schino, J. M. Kenny, and G. Abbruzzese, "Analysis of the recrystallization and grain growth processes in AISI 316 stainless steel," *Journal of Materials Science*, vol. 37, no. 24, pp. 5291–5298, Dec. 2002, doi: 10.1023/A:1021068806598.

[38] J. Xu, H. Brodin, R. L. Peng, V. Luzin, and J. Moverare, "Effect of heat treatment temperature on the microstructural evolution of CM247LC superalloy by laser powder bed fusion," *Materials Characterization*, vol. 185, p. 111742, Mar. 2022, doi: 10.1016/j.matchar.2022.111742.

[39] A. Keshavarzkermani *et al.*, "Static recrystallization impact on grain structure and mechanical properties of heat-treated Hastelloy X produced via laser powder-bed fusion," *Materials Characterization*, vol. 173, p. 110969, Mar. 2021, doi: 10.1016/j.matchar.2021.110969.

[40] S. Krog-Pedersen, J. R. Bowen, and W. Pantleon, "Quantitative characterization of the orientation spread within individual grains in copper after tensile deformation," *International Journal of Materials Research*, vol. 100, no. 3, pp. 433–438, Mar. 2009, doi: 10.3139/146.110032.

[41] M. Godec, S. Zaefferer, B. Podgornik, M. Šinko, and E. Tchernychova, "Quantitative multiscale correlative microstructure analysis of additive manufacturing of stainless steel 316L processed by selective laser melting," *Materials Characterization*, vol. 160, p. 110074, Feb. 2020, doi: 10.1016/j.matchar.2019.110074.

[42] M. Moyle, C. Ledermueller, Z. Zou, S. Primig, and N. Haghdadi, “Multi-scale characterisation of microstructure and texture of 316L stainless steel manufactured by laser powder bed fusion,” *Materials Characterization*, vol. 184, p. 111663, Feb. 2022, doi: 10.1016/j.matchar.2021.111663.

[43] S. Dryepondt, P. Nandwana, P. Fernandez-Zelaia, and F. List, “Microstructure and high temperature tensile properties of 316L fabricated by laser powder-bed fusion,” *Additive Manufacturing*, vol. 37, p. 101723, Jan. 2021, doi: 10.1016/j.addma.2020.101723.

[44] L. Lemarquis, P. F. Giroux, H. Maskrot, B. Barkia, O. Hercher, and P. Castany, “Cold-rolling effects on the microstructure properties of 316L stainless steel parts produced by Laser Powder Bed Fusion (LPBF),” *Journal of Materials Research and Technology*, vol. 15, pp. 4725–4736, Nov. 2021, doi: 10.1016/j.jmrt.2021.10.077.

[45] M. Laleh, A. E. Hughes, M. Y. Tan, G. S. Rohrer, S. Primig, and N. Haghdadi, “Grain boundary character distribution in an additively manufactured austenitic stainless steel,” *Scripta Materialia*, vol. 192, pp. 115–119, Feb. 2021, doi: 10.1016/j.scriptamat.2020.10.018.

[46] H. Yin, M. Song, P. Deng, L. Li, B. C. Prorok, and X. Lou, “Thermal stability and microstructural evolution of additively manufactured 316L stainless steel by laser powder bed fusion at 500–800 °C,” *Additive Manufacturing*, vol. 41, p. 101981, May 2021, doi: 10.1016/j.addma.2021.101981.

[47] D. Kong *et al.*, “About metastable cellular structure in additively manufactured austenitic stainless steels,” *Additive Manufacturing*, vol. 38, 101804, 2021, doi: 10.1016/j.addma.2020.101804.

[48] N. Ohkubo, K. Miyakusu, Y. Uematsu, and H. Kimura, “Effect of Alloying Elements on the Mechanical Properties of the Stable Austenitic Stainless Steel,” *ISIJ International*, vol. 34, no. 9, pp. 764–772, 1994, doi: 10.2355/isijinternational.34.764.

[49] P. Deng *et al.*, “On the thermal coarsening and transformation of nanoscale oxide inclusions in 316L stainless steel manufactured by laser powder bed fusion and its influence on impact toughness,” *Materials Science and Engineering: A*, vol. 835, p. 142690, Feb. 2022, doi: 10.1016/j.msea.2022.142690.

[50] F. J. Humphreys and M. Hatherly, *Recrystallization and Related Annealing Phenomena*. Elsevier, 2012.

[51] P. A. Beck and P. R. Sperry, “Strain Induced Grain Boundary Migration in High Purity Aluminum,” *Journal of Applied Physics*, vol. 21, no. 2, pp. 150–152, Feb. 1950, doi: 10.1063/1.1699614.

[52] A. Ariaseta, S. Kobayashi, M. Takeyama, Y. Wang, and S. Imano, “Characterization of Recrystallization and Second-Phase Particles in Solution-Treated Additively Manufactured Alloy 718,” *Metallurgical and Materials Transactions A*, vol. 51, no. 2, pp. 973–981, Feb. 2020, doi: 10.1007/s11661-019-05560-y.

[53] J. E. Bailey, P. B. Hirsch, and N. F. Mott, “The recrystallization process in some polycrystalline metals,” *Proceedings of the Royal Society of London. Series A. Mathematical and Physical Sciences*, vol. 267, no. 1328, pp. 11–30, Apr. 1962, doi: 10.1098/rspa.1962.0080.

[54] H. S. Zurob, Y. Bréchet, and J. Dunlop, “Quantitative criterion for recrystallization nucleation in single-phase alloys: Prediction of critical strains and incubation times,” *Acta Materialia*, vol. 54, no. 15, pp. 3983–3990, Sep. 2006, doi: 10.1016/j.actamat.2006.04.028.

[55] U. Scipioni Bertoli, B. E. MacDonald, and J. M. Schoenung, “Stability of cellular microstructure in laser powder bed fusion of 316L stainless steel,” *Materials Science and Engineering: A*, vol. 739, pp. 109–117, Jan. 2019, doi: 10.1016/j.msea.2018.10.051.

[56] P. A. Manohar, M. Ferry, and T. Chandra, “Five Decades of the Zener Equation,” *ISIJ International*, vol. 38, no. 9, pp. 913–924, 1998, doi: 10.2355/isijinternational.38.913.

[57] R. A. Varin, “Grain boundary diffusion and free energy during the recrystallization of type 316 stainless steel,” *Materials Science and Engineering*, vol. 66, no. 1, pp. 97–105, Sep. 1984, doi: 10.1016/0025-5416(84)90144-7.

[58] T. Delacroix, F. Lomello, F. Schuster, H. Maskrot, and J.-P. Garandet, “Influence of powder recycling on 316L stainless steel feedstocks and printed parts in laser powder bed fusion,” *Additive Manufacturing*, vol. 50, p. 102553, Feb. 2022, doi: 10.1016/j.addma.2021.102553.

[59] P. Faivre and R. D. Doherty, “Nucleation of recrystallization in compressed aluminium: studies by electron microscopy and Kikuchi diffraction,” *Journal of Materials Science*, vol. 14, no. 4, pp. 897–919, Apr. 1979, doi: 10.1007/BF00550722.

[60] H. E. Sabzi, E. Hernandez-Nava, X.-H. Li, H. Fu, D. San-Martín, and P. E. J. Rivera-Díaz-del-Castillo, “Strengthening control in laser powder bed fusion of austenitic stainless steels via grain boundary engineering,” *Materials & Design*, vol. 212, p. 110246, Dec. 2021, doi: 10.1016/j.matdes.2021.110246.

[61] S. Gao *et al.*, “Recrystallization-based grain boundary engineering of 316L stainless steel produced via selective laser melting,” *Acta Materialia*, vol. 200, pp. 366–377, Nov. 2020, doi: 10.1016/j.actamat.2020.09.015.